

Supplementary material

## **Multiscale structural analysis of defective graphene in transmission electron microscopy images using persistent homology**

Ryuto Eguchi<sup>1,2,a)</sup>, Ayako Hashimoto<sup>1,2,a)</sup>

<sup>1</sup>National Institute for Materials Science, 1-2-1 Sengen, Tsukuba, Ibaraki 305-0047, Japan

<sup>2</sup>Subprogram in Materials Science and Engineering, Degree Programs in Pure and Applied Sciences, Graduate School of Science and Technology, University of Tsukuba, 1-1-1 Tennodai, Tsukuba, Ibaraki 305-8577, Japan

<sup>a)</sup> Author to whom correspondence should be addressed: EGUCHI.Ryuto@nims.go.jp, HASHIMOTO.Ayako@nims.go.jp

### **S1. Cleaning process of graphene and HR-TEM observation condition**

After graphene transfer, the graphene sample was heated at 300 °C and  $8 \times 10^{-6}$  Pa for 2 h in a microscope column using a heating holder (Model 652, Gatan, Pleasanton, CA, USA) to remove surface contamination.

HR-TEM images were acquired using a spherical aberration coefficient of 5  $\mu\text{m}$ , semi-convergence angle of  $\geq 20$  mrad, defocus of  $-7$  nm, and exposure time of 2 s.

### **S2. Superlevel filtration on grayscale images and representative examples of g-PDs**

Superlevel filtration on grayscale images is performed by sequentially applying a series of pixel-intensity thresholds, as shown in Fig. S1. First, for a pixel image such as Fig. S1(a), the pixel intensities are normalized so that the brightest pixel is assigned a value of 255 and the darkest pixel a value of 0, as illustrated in Fig. S1(b). In the superlevel filtration of Fig. S1(b), the filtration starts from the maximum pixel intensity (255) as the initial threshold and successively decreases the threshold to the minimum intensity (0), filling all pixels with intensity greater than or equal to each threshold in white. Focusing on 0D holes (connected components), two holes appear at a threshold of 255 and merge at a threshold of 100 and accordingly, the birth and death values are 255 and 100, respectively. Since the lifetime is defined as the difference between the

birth and death times, the lifetime in this example is 155.

To demonstrate the relationship among the birth, death, and lifetime values, Fig. S2 shows the simulated grayscale images containing nine Gaussian peaks. In Fig. S2(a)–(c) (left panels), the maximum peak intensity is fixed at 255 while the background intensity is varied at 0, 100, and 200, respectively. Consequently, the birth values remain unchanged at 255, whereas the death values shift from 0 to 100 and 200, respectively, in the 0D g-PDs in (right panels). Accordingly, the lifetimes decrease from Fig. S2(a) to (c). In Fig. S2(d) (left), the background intensity is fixed at 0 and the image is constructed from three-type Gaussian peaks with intensity 200, 100, and 50. The g-PD exhibits three b–d pairs with different birth values, while all death values remain at 0 because the background intensity does not change. Therefore, the lifetimes also decrease in the order of peak height 200, 100, and 50.

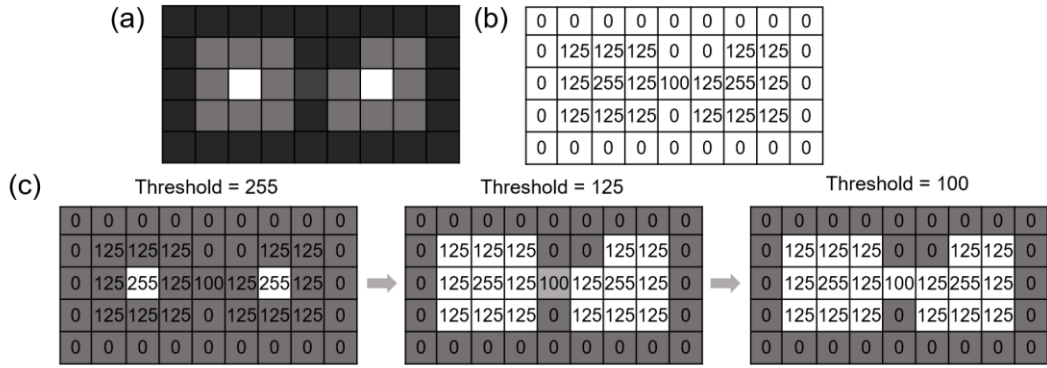


**Figure S1.** (a) 5×9-pixel grayscale image. (b) Corresponding intensity map normalized so that the brightest pixel is assigned to 255 and the darkest pixel to 0. (c) Superlevel filtration on the grayscale image in (a). The threshold successively decreases from 255 to 125 and 100, filling all pixels with intensity greater than or equal to each threshold in white. Two 0D holes appear at a threshold of 255 and merge at a threshold of 100.

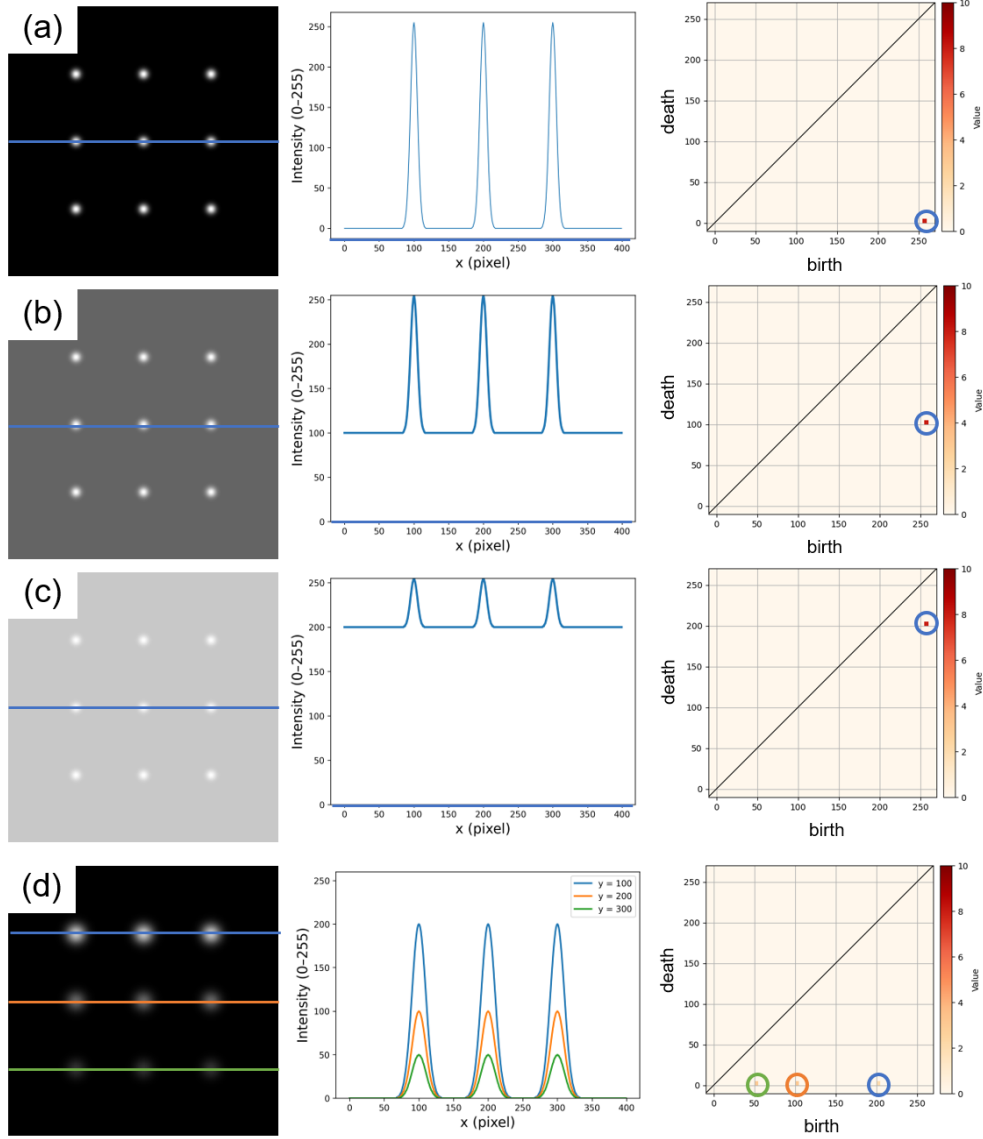


**Figure S2.** (a–c) Simulated grayscale images (left panels) containing nine Gaussian peaks with different background intensities and corresponding intensity profiles (middle panel) along the blue lines in the left images passing through the Gaussian centers. The background intensities are set to 0, 100, and 200, while the maximum value of all Gaussian peaks is fixed at 255. Resultant 0D g-PDs (right panels) containing b–d pairs with different death values. (d) Simulated grayscale image (left) containing three-type Gaussian peaks with intensity 200, 100, and 50 (background intensity is set to 0) and corresponding intensity profiles (middle) along the blue, orange, and green lines in the left image passing through the peak center. Resultant 0D g-PD (right) containing three b–d pairs with different birth values.

### S3. Comparison between raw and Gaussian-filtered HR-TEM images

At the initial step in Fig. 1, we applied Gaussian filtering to experimental HR-TEM images. Fig. S3(a) and (b) show part of the image at  $t_1$  before and after filtering, respectively. The operation employed OpenCV's Gaussian Blur function<sup>1</sup> with a  $15 \times 15$  kernel and standard deviation of 3 pixels. The white dot-like noise in Fig. S3(a) decreased markedly after filtering, as shown in Fig. S3(b).

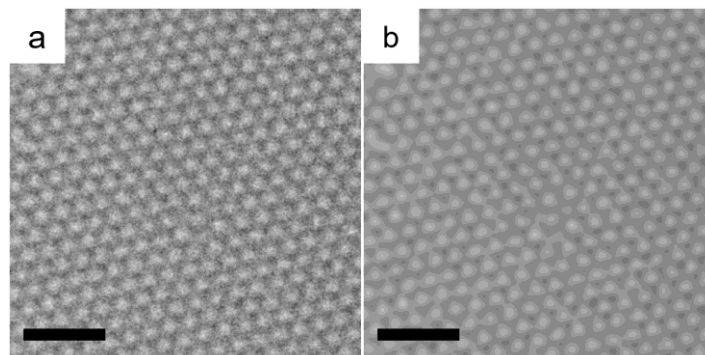


**Figure S3.** (a) Raw HR-TEM image of graphene, cropped from Fig. 2(b). (b) Gaussian-filtered image of (a). Scale bars represent 1 nm.

### S4. Computation of carbon-atom positions using birth points and comparison between experimental and simulated TEM images

Fig. S4 shows the detailed extraction process of carbon-atom positions following the pipeline in Fig. 2(a)–(c). The red points in Fig. S4(a) show birth points, i.e., the pixel with maximum intensity closely indicating the centers of the carbon-atom polygons. The black points in Fig. S4(b) correspond to the Voronoi vertices of the birth points in Fig. S4(a). The obtained Voronoi diagrams were computed via Lloyd's structural relaxation to regard the Voronoi vertices of the Voronoi diagrams as carbon-atom positions. At each step, the diagram was constructed from the current generator (site) points using SciPy's `scipy.spatial.Voronoi`.<sup>2</sup> The generators were then relocated to the centroid of their finite cells (unbounded cells discarded), and the final diagram was recomputed from the relaxed generators. As the number of iterations is a parameter, we set it to three to achieve stabilization of the birth points. After only one or two iterations, some Voronoi points remained excessively close to each other, whereas beyond the fourth iteration, the position of the Voronoi points exhibited negligible displacements compared with those after the third iteration. We confirmed that three iterations are sufficient to achieve a stable relaxation without excessive computational cost. The calculated Voronoi vertices were considered to be the positions of the carbon atoms. Thus, the black points in Fig. S4(b) were calculated through PH from the image contrast without consideration of any chemical or physical information for carbon atoms. To

incorporate such realistic effects, we additionally conducted structure relaxation of the Voronoi vertex distribution in Fig. S4(b) using an MD calculation, as shown in Fig. S4(c). Structural relaxation was performed with the Atomic Simulation Environment (ASE)<sup>3</sup> using LAMMPS as the back-end engine.<sup>4</sup> The AIREBO interatomic potential was employed<sup>5</sup> and the geometry was optimized with the Fast Inertial Relaxation Engine (FIRE).<sup>6</sup> Convergence was defined by a maximum atomic force below 0.01 eV Å<sup>-1</sup>. The relaxation process removed the unexpected short C–C bonds indicated by red arrows in Fig. S4(b). Finally, we simulated a TEM image from the Voronoi vertex distribution after the relaxation using abTEM software<sup>7</sup> to confirm the validity of the atomic arrangements obtained through PH and Voronoi vertex calculations. Fig. S4(d) compares the experimental and simulated TEM images. No significant differences between these images were observed. We therefore concluded that the birth points extracted in Fig. 1 captured the vicinity of carbon-atom polygon centers and the positions of carbon atoms could be determined from the birth points through Voronoi calculation.

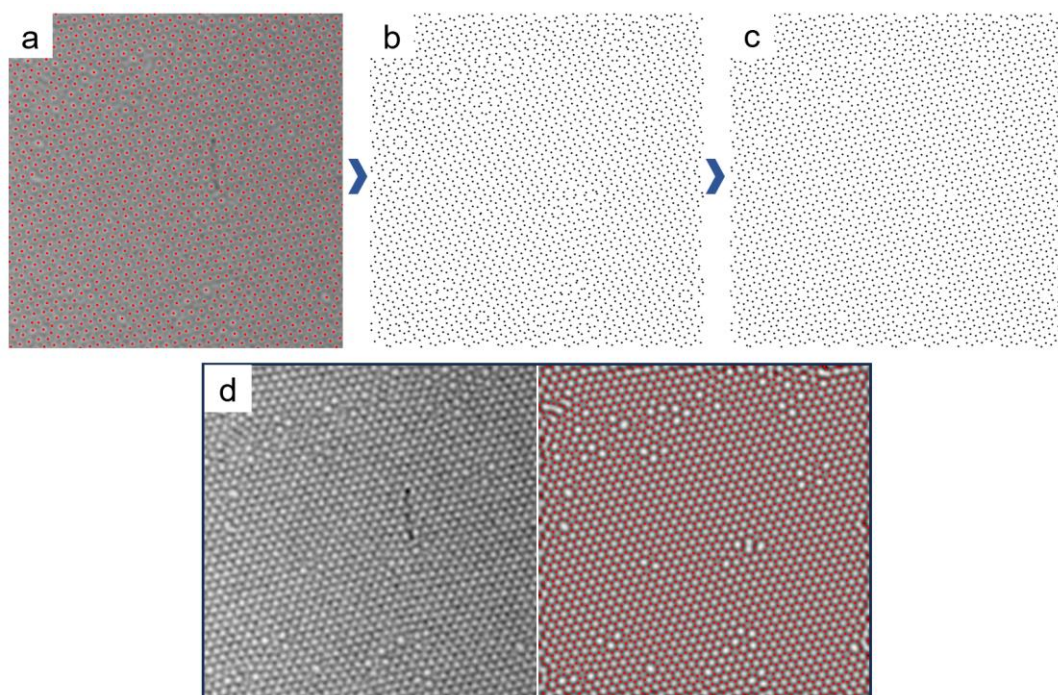


**Figure S4.** (a) Enlarged TEM image from Fig. 2(b) overlaid with birth points (red points) obtained through the strategy in Fig. 1(a)–(c). (b) The distribution of Voronoi vertices (black points) calculated from the birth points in (a); i.e., point clouds. (c) Relaxed atomic structure of the distribution of Voronoi vertices in (b) obtained by molecular dynamics calculation. (d) Experimental TEM image (same as in (a), left) and simulated TEM image calculated from the atomic arrangement in (c) (right). The overlaid atomic arrangement is shown as red points. Scale bar is 2 nm.

## S5. Separation of linked holes via the watershed method

In Fig. 2(d), the area distribution of the extracted zero-dimensional (0D) holes has several peaks. The second and higher peaks above  $0.038 \text{ nm}^2$  includes linked holes, as shown in the left panels of Fig. S5(a)–(c). The threshold of  $0.038 \text{ nm}^2$  was determined by fitting the histogram of the area distribution (restricted to area  $\leq 0.07 \text{ nm}^2$ , covering the tail of the second peak) with a two-component Gaussian mixture model. The intersection point between the two fitted Gaussian components corresponds to the local minimum of the mixture distribution between the peaks, which was defined as the threshold in this calculation. Holes corresponding to the areas  $\leq 0.038 \text{ nm}^2$  were predominantly isolated, whereas those  $\geq 0.038 \text{ nm}^2$  were all linked holes, as shown in the inset of Fig. 1(e).

The first goal of this study was to extract the region enclosed by a single carbon-atom polygon. To achieve this, the linked holes shown in the left panels of Fig. S5 need to be separated properly. We applied the watershed transform to a binarized image in which the extracted regions of the linked holes were black and all other regions were white.<sup>1</sup> In the watershed segmentation, small spurious peaks with areas  $< 0.005 \text{ nm}^2$  were excluded in advance, and the distance transform was computed using a mask size of 3 (Euclidean metric). In addition, the relative ratio  $r$  directly controls which local

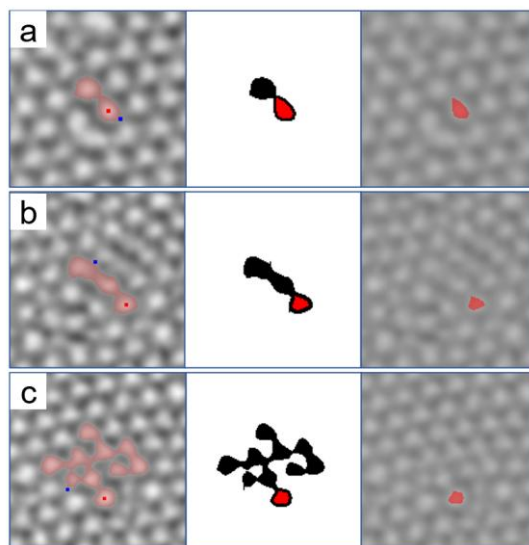


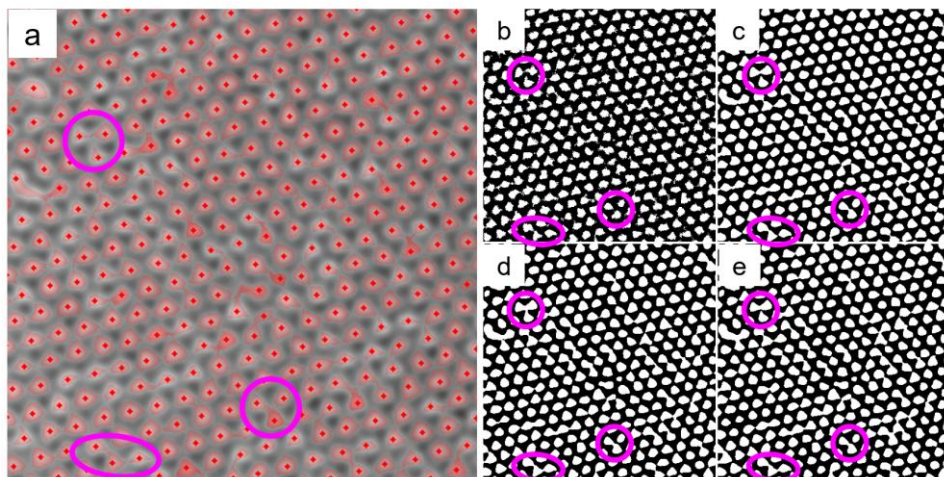
**Figure S5.** (a)–(c) Separation of linked zero-dimensional holes in TEM images of defective graphene using the watershed method. (Left panels) Linked holes obtained via inverse analysis of g-PD in Fig. 1(b) under the constraint that each hole area exceeds  $0.0038 \text{ nm}^2$ . Red and blue points represent birth and death points, respectively. (Middle panels) Separated and colored regions of the linked holes in the left panels. The red regions indicate the separated holes with the birth points in the left panels. (Right panels) Separated holes (red) overlaid on the TEM images.

peaks in the distance-transform image are regarded as seeds: larger  $r$  selects only the highest peaks (fewer seeds), whereas smaller  $r$  admits lower peaks as well (more seeds, including possible noise). Seed regions (markers) were therefore determined by thresholding the distance map at relative ratios  $0.2 < r < 0.6$  of the maximum distance, with an increment of 0.01. The optimal  $r$  was defined as the value yielding the largest number of black regions. Seeds obtained at this  $r$  were then used as the initialization for the watershed algorithm. In this procedure, the mask size and  $r$  range in the optimization are treated as hyperparameters. Their validity was empirically confirmed by visually comparing the shapes and extents of the segmented regions derived from the linked 0D holes with those of the corresponding contrast in the original TEM images (Fig. S5). Blind or arbitrary selection of these hyperparameters can compromise the segmentation: if the mask size and  $r$  are set too small, over-segmentation occurs producing unrealistically small and fragmented regions; conversely, if they are set too large, the watershed transform would fail to separate the linked holes, leaving them identical to the original connected regions. After the transformation, several isolated regions were obtained from which only the region with the birth point (red points in the left panels of Fig. S5) was extracted, as shown in red in the middle panels. In the right panels of Fig. S5, the colored separated regions are overlaid on the corresponding TEM images, demonstrating the successful extraction of the regions enclosed by a single carbon-atom polygon.

## **S6. Comparison of extraction of 0D holes via the present PH pipeline with a representative binarization method**

Here we compare extraction of 0D holes via PH with a conventional representative binarization method often used for such extractions. In the PH-based extraction result shown in Fig. S6(a), the regions indicated by pink circles can be extracted as three holes. In contrast, in the binarization method results with different kernel sizes, as shown in Fig. S6(b)–(e), the marked regions are difficult to recognize as three holes. An adaptive threshold function in OpenCV was used for binarization.<sup>1</sup> In Fig. S6(b), the surrounding region contains more than three holes with different sizes because of the presence of numerous dots originating from noise. In Fig. S6(c)–(e), the dot-like noise is decreased and the white domains are highly interconnected; consequently, the surrounding regions contained fewer than three holes.





**Figures S6** Comparison of zero-dimensional hole extraction via PH with a representative binarization method. (a) Zero-dimensional hole extracted via PH following the pipeline in Figs. 1(a)-(c), (e). Red points show birth points distribution (Fig. 1(c)). The regions marked by pink circles successfully contains three holes with three birth points. (b)-(e) Binarized images of a gaussian-filtered TEM image with different kernel sizes: 9 for (b), 49 for (c), 99 for (d) and 399 for (e) in an adaptive threshold method. Scalebars represents 0.5 nm.

## S7. Roundness calculation and correspondence between example shapes and their roundness values

We calculated the ring roundness ( $R$ ) from the average birth value in b-PDs. Here,  $R$  is defined as  $R = A / (\pi b_{ave}^2)$ , where  $A$  is the area of the extracted hole and  $b_{ave}$  denotes the average birth value in b-PDs. The birth value corresponds to the half of the object length measured along the minor axis, which can be explained from the filtration principle of binarized images.<sup>8</sup> As examples of ideal objects, a circle and ellipse are depicted in Fig. S7(a), where their birth values in b-PDs correspond to the radius and semi-minor axis length, respectively. That is,  $R$  is 1 for a circle and exceeds 1 for an ellipse. Fig. S7(b) shows three ellipses with different degrees of distortion along with their calculated  $R$ . For the ideal ellipses,  $R$  increases with hole distortion. In Fig. S7(c) and (d), we present the computed PDs of the actual 0D holes (inset) on an identical scale to that of an experimental TEM image. The holes were binarized to form black regions. The average birth value of the 0D hole in Fig. S7(d) is larger than that in Fig. 5(c). Consistently, the 0D hole in Fig. S7(d) appears to have slightly larger width along the minor axis and appears more elongated than that in Fig. S7(c). Thus,  $b_{ave}$  and  $R$  can be used to quantitatively evaluate the shape of objects; e.g., holes.



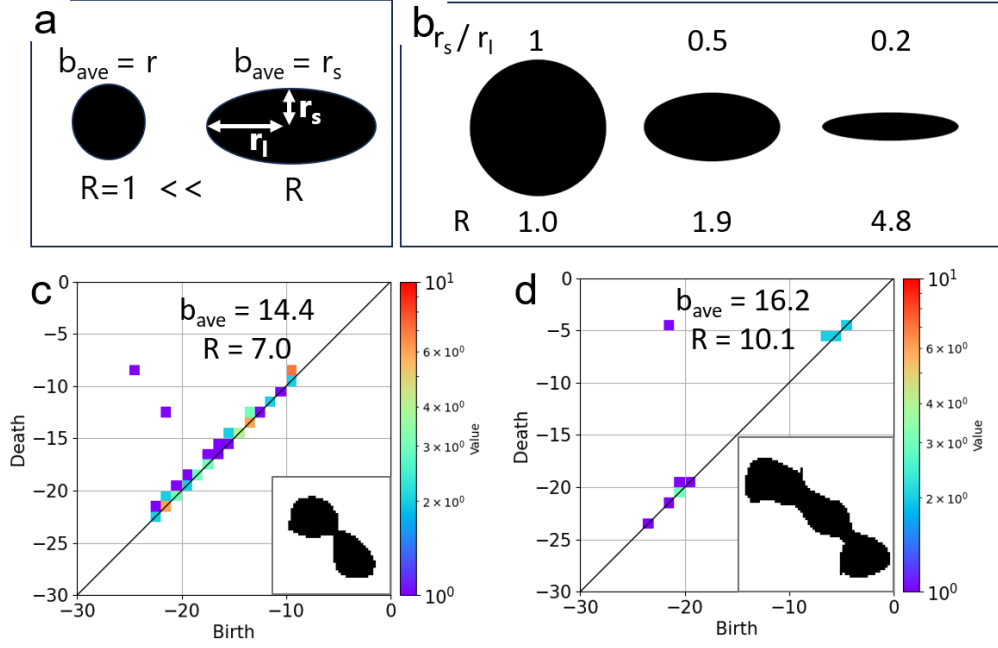


**Figure S7.** Geometrical interpretation of roundness  $R$ . (a) A perfect circle and ellipse as ideal examples. Here, the birth values in the b-PDs correspond to the radius for a circle and semi-minor axis length for an ellipse. (b) Three ellipses with different ratios of minor- and major-axis length and corresponding  $R$  values. (c), (d) Actual OD holes extracted from an experimental TEM image by inverse analysis (insets), and their OD b-PDs. Calculated average  $b_{ave}$  and  $R$  values are shown.

### S8. Calculation of polygon number $N$ using Voronoi diagrams constructed from birth point distributions

We calculated polygon number  $N$  from birth point distributions. As mentioned in Supplementary Material S4, the birth points are located near the carbon-atom polygon centers. Therefore, we calculated  $N$  by considering the focal birth point and its enclosed Voronoi diagram. For example, we considered the focal birth points indicated by red circles (left panels of Fig. S8(a) and (b)). Firstly, as shown in the middle panels, Voronoi diagrams were constructed from the birth point distributions (left panels). Second, each Voronoi cell enclosing a focal birth point was filled in black, and the Voronoi edges were then removed, as shown in the right panels. We counted the number of isolated black regions in the right panels and the number of Voronoi vertices before the filling operation. Here, one isolated black region refers to a domain consisting of both filled black areas and Voronoi vertices. Finally, defining the number of the isolated black regions as  $N_{\text{isolated regions}}$  and the number of the Voronoi vertices as  $N_{\text{Voronoi vertices}}$ , we calculated  $N$  as follows,

$$N = N_{\text{Voronoi vertices}} - N_{\text{isolated regions}} + 1. \quad (\text{S1})$$

For example, for the birth point surrounded by the red circles as a representative point of each polygon,  $N$  in Fig. S8(a) and (b) were calculated to be 6 and 5, respectively.

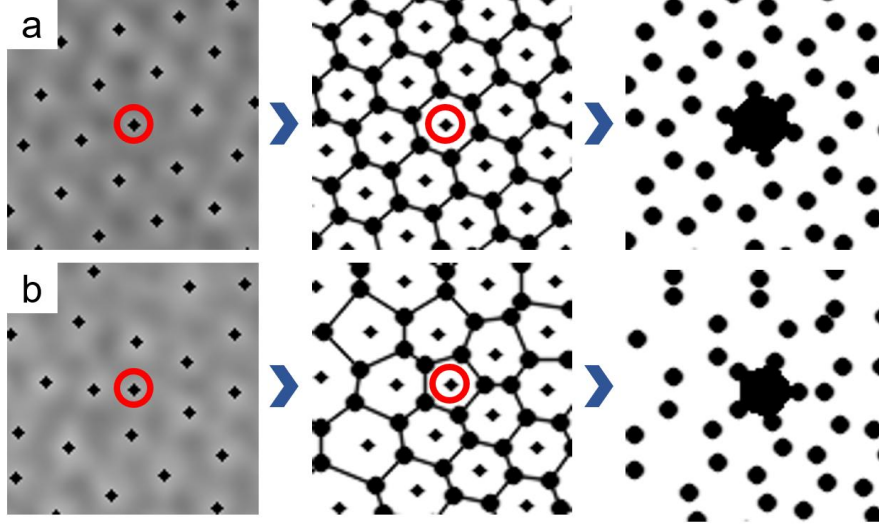


**Figure. S8.** (a), (b) Calculation of polygon number  $N$ . (Left panels) Birth point distribution with focal birth points indicated by red circles. (Middle panels) Voronoi vertices (circles) and edges (lines) from the birth points. (Right panels) Voronoi vertices and filled black region bounded by Voronoi edges, which were removed.

### S9. Representative holes obtained from g-PD inverse analysis and $R$ values

Ideally, roundness  $R$  is 1 for a perfect circle, and approximately 1.10 for a regular hexagon because a regular hexagon with side length  $a$  has area  $A = 3\sqrt{3}/2 a^2$  and radius  $r = \sqrt{3}/2 a$ , which yields  $R = A / (\pi b_{\text{ave}}^2) = 2\sqrt{3}/\pi \approx 1.10$ . However, actual  $R$  values are larger than that of an ideal hexagon and can exceed 7. Fig. S9(a) and (b) show actual hexagonal holes with different  $R$  extracted from an experimental image using g-PD inverse analysis. In Fig. S9(a), the hole with  $R = 1.63$ , which is close to the distribution peak value (Fig. 3(h)), has a small spur-like protrusion. Holes with such protrusions can be seen in the experimental TEM images. The protrusions produce larger  $R$  than that of an ideal regular hexagon. In Fig. S9(b), the residually connected holes, which exist even after the separation (Supplementary Material S5), have large  $R$  values of more than 7.

It should be noted that  $R$  values reflect not only intrinsic structural changes but also extrinsic observation factors such as aberrations or focus shift. Fig. S9(c) and (d) show simulated images of perfect graphene without and with two-fold astigmatism, respectively. Fig. S9(c) shows a round carbon-atom polygon with a vacuum region exhibiting  $R=1.17$ , which is close to 1.10 for an ideal hexagon. In contrast, Fig. S9(d)

shows a distorted vacuum region with larger  $R$ . Thus, two-fold astigmatism distorts vacuum regions, resulting in larger  $R$ . In addition, other aberrations such as defocus, coma, and three and four-fold aberration may also exist in the experimental images and affect  $R$ .

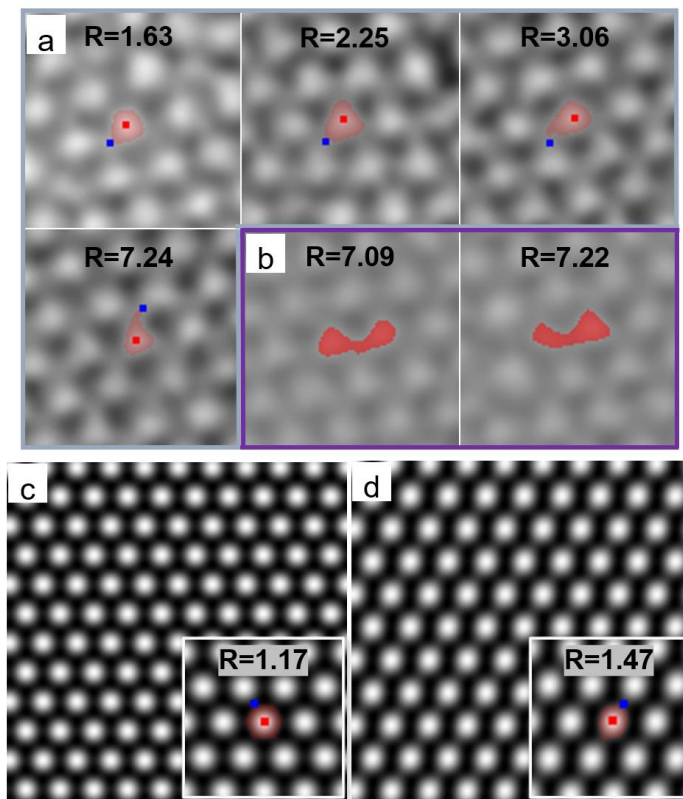


**Figure S9.** (a) and (b) Representative hexagonal holes with different  $R$  (red regions) extracted from an experimental image by g-PD inverse analysis. (a) Holes obtained without any separation procedure (Supplementary Material S3). (b) Holes obtained after separation. Simulated TEM images of perfect hexagons (c) without and (d) with two-fold astigmatism. Representative holes obtained by g-PD inverse analysis and calculated  $R$  values are shown in insets.

### S10. Average $R$ value and its standard deviation

We conducted selective analysis of holes arising from hexagons versus those from defects by using both  $R$  and  $N$  values. Table S1 summarizes the average  $R$  value and its standard deviation for each  $N$ -polygon. As mentioned in the main text, the  $N$ -selective  $R$  values highlight several important observations: First,  $R$  values of hexagonal and non-hexagonal polygons are different, suggesting that electron irradiation generates defects that lead to more distorted polygons than the hexagons in as-prepared graphene. Additionally, the standard deviation increases with  $N$ , indicating that heptagons are more prone to geometric distortion than pentagons.

**Table S1.** Average  $R$  value and its standard deviation for each  $N$ -polygon at  $t_0$ ,  $t_1$ , and  $t_2$ .

Polygon number $N$	Average $R$ at $t_0$ (Standard deviation)	Average $R$ at $t_1$ (Standard deviation)	Average $R$ at $t_2$ (Standard deviation)
5 (pentagon)	---	3.37 (5.38)	2.86 (2.78)
6 (hexagon)	3.49 (7.40)	3.72 (8.01)	5.14 (7.12)
7 (heptagon)	---	6.09 (10.65)	7.73 (17.85)
Average	3.49(7.40)	3.79(8.00)	5.12(8.13)

### S11. Determination of b-d pairs used for inverse analysis and optimization of noise bandwidth parameter $\varepsilon$ to calculate stable volume

We performed inverse analysis of the selected b-d pairs in the p-PDs only from hexagonal polygons (Step 1 in Algorithm S1). First, the thresholds for selection of b-d pairs were determined using the 1D p-PD of as-prepared graphene. Here, the inverse analysis of the 1D PD mostly generated small triangles, because every point has two neighboring points and can satisfy the condition that the three points are not collinear. However, larger rings than the small triangles are important for focusing on defect connectivity because of their larger death and lifetime values. Therefore, the b-d pairs with three vertices were extracted. Next, the maximum death and lifetime among these pairs were measured to determine the corresponding thresholds. We then selected the b-d pairs above the death and lifetime thresholds to select the larger rings.

Next, we determined the free parameter  $\varepsilon$  for each b-d pair (Step 2 in Algorithm S1).  $\varepsilon$  is a noise bandwidth parameter and plays a role in controlling noise robustness. When  $\varepsilon$  is small (e.g., approaching zero), the computed ring tends to have relatively large volume and remains highly sensitive to noise. Conversely, as  $\varepsilon$  increases, the ring becomes more robust to noise, but may eliminate important structural information. Therefore,  $\varepsilon$  must be tuned when we calculate the stable volume when mapping a ring onto a real space. In Algorithm S1, Step 2 roughly includes two procedures: Step 2.1 is searching for a stable  $\varepsilon$  value and Step 2.2 is prohibiting the rings from having longer edges than the distance between the centers of polygons. In Step 2.1, to identify a stable  $\varepsilon$ , we swept  $\varepsilon$  from the minimum pixel length (0.01065 nm) to the lifetime and computed the number of vertices for each b-d pair. Then, we considered the smallest  $\varepsilon$  as the start of the plateau in the curve of the number of vertices against  $\varepsilon$ . As an exceptional case, if the maximum number of vertices during an  $\varepsilon$  sweep was less than eight, the b-d pair was discarded to ensure efficient detection of defect clusters including more than two non-hexagonal points. The reason why we should discard the rings with eight vertices is that the smallest defect cluster composed of two pentagons has eight vertices. Another exceptional case is that when the number of vertices in the

longest plateau is less than eight, we use the smallest  $\epsilon$  for eight vertices. In Step 2.2, we removed the rings with longer edges than the distance between the centers of polygons because they could be oversimplified rings, that is, small rings composed of the vertices of a larger ring, as shown in Fig. S10. In a regular hexagonal point cloud with nearest-neighbor distance  $d$ , the next-nearest neighbor is  $\sqrt{3}d \approx 1.73d$ . Therefore, edges longer than approximately  $1.5d$  are likely to constitute shortcuts, as visualized in Fig. S10. Using the  $\epsilon$  determined in Step 2.1, we calculated the maximum distance between adjacent vertices on a ring. If the distance exceeded the  $1.5d$  between hexagonal centers of as-prepared graphene, we swept  $\epsilon$  from the previous  $\epsilon$  calculated in Step 2.1 to the minimum pixel length. We repeated this operation until the condition to determine the optimal  $\epsilon$  was satisfied.

---

**Algorithm 1:** Selection of b-d pairs for inverse analysis and setting of  $\epsilon$  in stable volume computation

---

**Step 1: Selection of b-d pairs for inverse analysis**

Output one-dimensional p-PD for pointcloud of birth points at  $t_0$  of pristine graphene.

**for Each b-d pair do**

    Compute the stable volume and obtain the number of vertices.

Identify the maximum death and lifetime among b-d pairs with the number of vertices = 3.

Select b-d pairs whose death and lifetime exceed these thresholds for inverse analysis.

**Step 2: Setting the  $\epsilon$  value for each b-d pair in stable volume computation**

**for Each selected b-d pair do**

    Let lifetime be  $l$ .

    Set resolution  $r = 0.105$  nm (pixel size in TEM image).

    Choose  $\epsilon$  in  $[r, l]$  as follows:

    // Step 2.1: Sweep  $\epsilon$  and detect plateau

    Sweep  $\epsilon$  in steps of  $r$  over  $[r, l]$  and compute ring size changes.

    Identify the longest plateau in the ring size vs.  $\epsilon$  curve.

    Select the smallest  $\epsilon$  at the start of this plateau.

**if multiple longest plateaus then**

        Choose the one starting at the smaller  $\epsilon$ .

**else**

        // Exceptions

**if maximum ring size in the ring size variation  $< 8$  then**

        Discard the pair.

**if maximum ring size in the ring size variation  $\geq 8$  and plateau ring size  $< 8$  then**

        Choose the first  $\epsilon$  where ring size becomes 8.

    Denote the obtained  $\epsilon$  here as  $\epsilon_{\text{base}}$ .

    // Step 2.2: Refine  $\epsilon$  based on vertex distances

    From  $\epsilon_{\text{base}}$ , decrease  $\epsilon$  in steps of  $r$ .

    At each step, compute the maximum distance between adjacent vertices on the ring.

    Stop when this distance  $< 1.5 \times$  the hexagon center-to-center distance in ideal graphene.

    Use this  $\epsilon$  for stable volume computation.

**if condition not met at  $\epsilon = r$  then**

        Discard the pair.

---

**Algorithm S1.** Algorithm to determine the b-d pairs used for inverse analysis and optimize parameter  $\epsilon$  for calculating stable volume.

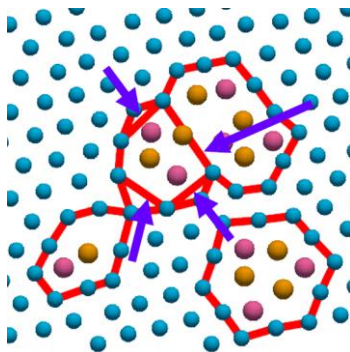


**Figure S10.** Inverse-analysis results from the 1D p-PD of the downsampled point cloud. Red rings were computed with unoptimized  $\varepsilon$ . The shortcut indicated by the blue arrow—an edge longer than the nearest-neighbor distance between hexagon centers—can be seen without  $\varepsilon$  optimization due to the smaller rings.

## S12. Effect of edges on the inverse analysis results

In Figs 4(g) and (h), some points arising from defects (shown in pink, orange, and deep blue) are not enclosed by any ring. The rings enclosing those points were recovered by adding hexagonal points around the original hexagonal points (light blue). In Fig. S11(b), outer-edge points were added to Fig. S11(a) (the same image as Fig. 4(g)), and inverse analysis was conducted with Algorithm S1. As a result, new enclosing rings emerged, which are defect clusters that were not detected in Fig. S11(a). However, several non-hexagonal points are still not enclosed in Fig. S11(b) (indicated by red arrows). In our algorithm (see Supplementary Materials S7), we discard the rings with less than eight vertices. The defect points without enclosing rings seem to have fewer than eight neighbors in their vicinity and were therefore intentionally excluded from the inverse analysis. In this way, one isolated non-hexagonal polygon is automatically excluded, leading to identification of clusters including more than two non-hexagonal polygons.



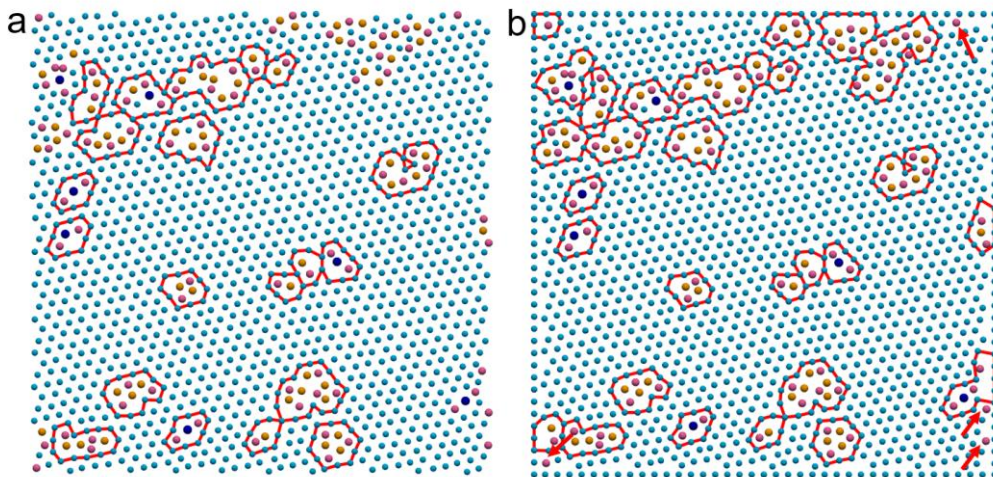


**Figure S11.** Inverse analysis results from the 1D p-PD of the downsampled point cloud (a) before and (b) after artificially adding hexagonal points. (a) is identical to Fig. 4(g). In (b), regularly spaced hexagonal points from the point cloud were added to (a). Defect clusters that were not detected in (a) are captured in (b). Several non-hexagonal points were not captured (indicated by red arrows) owing to the algorithm’s design (see Algorithm S1).

### S13. Effect of optimization of noise bandwidth parameter $\varepsilon$ on inverse analysis results

We optimized  $\varepsilon$  in the inverse analysis of the selected b-d pairs, as explained in Supplementary Materials S7. Fig. S12(a) shows inverse analysis results using optimized  $\varepsilon$ , which is the same as Fig. 4(g) (upper) and (h) (lower). The panels in Fig. S12(b)–(d) show inverse analysis results for the b-d pairs using  $\varepsilon$  values different from optimized  $\varepsilon$ ; i.e., (b) 0.01, (c) 0.05, and (d) 0.1 times the lifetime, which are within the  $\varepsilon$  range reported by Obayashi<sup>9</sup> for obtaining reliable inverse analysis results. In Fig. S12(b)–(d), redundant rings appear and the large rings fragment into multiple small rings, as indicated by black arrows in Fig. 4(g) (both upper and lower). In particular, at 0.01 times the lifetime parameter, the ring exhibits redundant detours. Thus, the optimization process of  $\varepsilon$  is important to extract rings with suitable size—neither excessively complex nor overly simple—leading to accurate capture of defect-cluster shape.

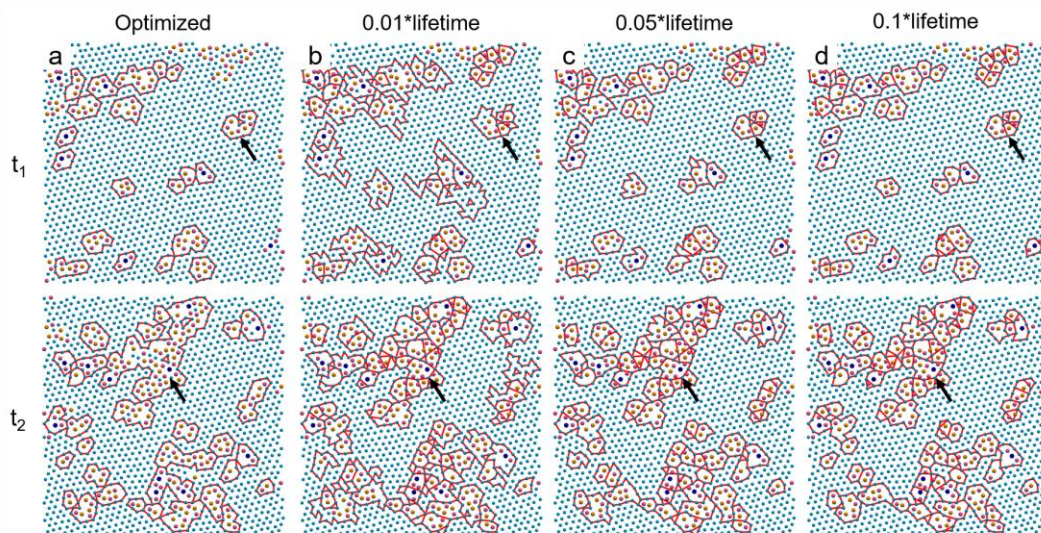


**Figure S12.** Inverse analysis results obtained from the 1D p-PD of a downsampled point cloud with different  $\varepsilon$  values. (a) Optimized  $\varepsilon$ . The results are the same as in Fig. 4(g) for  $t_0$  and (h) for  $t_1$ . (b) 0.01, (c) 0.05, and (d) 0.1 times the lifetime.

## REFERENCES

- <sup>1</sup> G. Bradski, “The OpenCV Library,” *Dr. Dobb’s Journal of Software Tools* (2000).
- <sup>2</sup> P. Virtanen *et al.*, “SciPy 1.0: Fundamental Algorithms for Scientific Computing in Python,” *Nat. Methods* **17**, 261–272 (2020).
- <sup>3</sup> A.H. Larsen *et al.*, “The atomic simulation environment—a Python library for working with atoms,” *J. Phys.: Condens. Matter* **29**, 273002 (2017).
- <sup>4</sup> A.P. Thompson *et al.*, “LAMMPS—a flexible simulation tool for particle-based materials modeling at the atomic, meso, and continuum scales,” *Comput. Phys. Commun.* **271**, 108171 (2022).
- <sup>5</sup> S. J. Stuart, A. B. Tutein, and J. A. Harrison, “A reactive potential for hydrocarbons with intermolecular interactions,” *J. Chem. Phys.* **112**, 6472–6486 (2000).
- <sup>6</sup> E. Bitzek, P. Koskinen, F. Gähler, M. Moseler, and P. Gumbsch, “Structural relaxation made simple,” *Physical Review Letters* **97**, 170201 (2006).
- <sup>7</sup> J. Madsen and T. Susi, “The abTEM code: transmission electron microscopy from first principles,” *Open Research Europe* **1**, 24 (2021).
- <sup>8</sup> R. Eguchi, Y. Wen, H. Abe, and A. Hashimoto, “Interpretable structural evaluation of metal-oxide nanostructures in scanning transmission electron microscopy (STEM) images via persistent homology,” *Nanomaterials* **14**, 1413 (2024).
- <sup>9</sup> Obayashi, I., “Stable volumes for persistent homology,” *J. Appl. Comput. Topol.* **7**, 671–706 (2023).